Check for updates

APPLIED SCIENCES AND ENGINEERING

Neuromorphic olfaction with ultralow-power gas sensors and ovonic threshold switch

Mingu Kang[1]†, Joon-Kyu Han[2]†, Kichul Lee[1]†, Jaeseok Jeong[1], Chanyoung Yoo[3], Jeong Woo Jeon[2], Byongwoo Park[2], Wonho Choi[2], Junseong Ahn[4], Kuk-Jin Yoon[1], Cheol Seong Hwang[2]*, Inkyu Park[1]*

Copyright © 2025 The Authors, some rights reserved; exclusive licensee American Association for the Advancement of Science. No claim to original U.S. Government Works. Distributed under a Creative Commons Attribution NonCommercial License 4.0 (CC BY-NC).

With increasing demand for gas sensors in mobile devices, research on developing an electronic nose (E-nose) is actively conducted. However, conventional E-nose systems based on von Neumann computing have encountered challenges such as high hardware costs and power consumption because of the necessity of hardware-intensive circuits and processors. This work implements low-power artificial olfactory neuron modules within a spiking neural network (SNN) to address this issue. The artificial olfactory neuron module is developed by connecting a GeSe-based ovonic threshold switch and a micro–light-emitting diode (μLED) platform–based semiconductor metal oxide gas sensor in series. The use of μLED gas sensors enables ultralow-power operation, resulting in substantially decreased power consumption. The artificial olfactory neuron module generates spike signals with low operation voltage, demonstrating energy efficiency and advanced performance. A real-time gas classification based on the SNN is feasibly conducted with an accuracy of 99.6%. Moreover, it is possible to classify different ingredients under humidity disturbance conditions through a hardware SNN.

INTRODUCTION

The rapid development of the internet of things and mobile platforms, such as smartphones and wearable devices, increasingly requires smaller mobile gas sensors to monitor environmental conditions. These sensors are used in various applications, including industrial safety, health care, air quality monitoring, and food monitoring (*1*–*3*). Chemoresistive-type gas sensors, well suited for miniaturized applications, have garnered considerable attention in meeting these demands (*4*, *5*). Consequently, various studies are underway to enhance their performance, with a primary focus on improving selectivity, which has been a notable challenge (*6*–*11*). In particular, research aimed at improving selectivity using an electronic nose (E-nose), inspired by the biological olfactory system, is emerging as an essential field (*12*). The biological olfactory system detects odor molecules through numerous olfactory receptors in the olfactory epithelium, a thin tissue at the top of the nasal cavity (*13*). These receptors respond specifically to different odor molecules, generating distinct electrical spike signals. These signals are then transmitted to mitral cells in the olfactory bulb, where the signal patterns are analyzed and relayed to the brain's olfactory cortex for the identification of odors (*14*).

Inspired by the biological olfactory mechanism, the E-nose can be developed by constructing a sensor array composed of multiple types of sensors and analyzing the sensing signal patterns collected from the array using machine learning or artificial intelligence (*15*–*18*). However, it is essential to preprocess the sensor signal to conduct pattern analysis using machine learning, as the raw sensor signal is in analog form. Therefore, analog-to-digital converters (ADCs) are necessary to convert the analog signals from the sensor array into digital form for further processing. In addition, von Neumann computing–based processor and memory must be used in the E-nose for the pattern analysis. The primary issues with using ADCs and the von Neumann computing architecture are high power consumption and hardware costs (*19*–*21*). Furthermore, as the number of gas sensors increases and the sensor signal range expands, the number of required ADCs also increases, leading to a more complex conversion circuit and even higher power consumption. The frequent data transfers between the processor and memory in von Neumann computing systems cause data transmission bottlenecks, which also increase power consumption (*19*, *22*). Given that the high hardware costs and power consumption problems are critical for mobile devices, conventional E-noses have limitations in applying them to mobile gas monitoring platforms (*15*, *16*). Similar limitations also arise in vision and touch sensor systems that emulate human sensory organs.

Therefore, research on implementing in-sensor computing based on neuromorphic sensor devices with spiking neural network (SNN) architecture is actively being conducted to overcome these bottlenecks (*21*, *23*–*30*). An artificial olfactory neuron module that simultaneously performs gas detection and spike encoding was developed to implement an in-sensor computing–based E-nose (*29*). It was composed of the metal oxide semiconductor field-effect transistor (MOSFET)–based neuron and the microheater platform–based semiconductor metal oxide (SMO) gas sensor (*15*, *31*). However, it had a relatively high operation voltage of 7.5 V to induce impact ionization in the MOSFET, which triggers threshold switching. In addition, despite using a microelectromechanical system–based microheater platform, the SMO gas sensor still demanded a relatively high power consumption of 12.9 mW for heating. Therefore, to further enhance the energy efficiency of the neuromorphic nose system, it is necessary to use a low-power SMO sensor platform and incorporate neuron devices with low operation voltage.

This study proposes a neuromorphic olfaction system based on a low-power artificial olfactory neuron module, which decreases the

[1]Department of Mechanical Engineering, Korea Advanced Institute of Science and Technology (KAIST), Daejeon 34141, Republic of Korea. [2]Department of Materials Science and Engineering and Inter-University Semiconductor Research Center and Inter-University Semiconductor Research Center, Seoul National University, Seoul 08826, Republic of Korea. [3]Department of Materials Science and Engineering, Hongik University, Seoul 04066, Republic of Korea. [4]Department of Electro-Mechanical Systems Engineering, Korea University, Sejong 30019, Republic of Korea. *Corresponding author. Email: inkyu@kaist.ac.kr (I.P.); cheolsh@snu.ac.kr (C.S.H.) †These authors contributed equally to this work.

Downloaded from https://www.science.org at Korea University on September 28, 2025

operation voltage of the neuron device and substantially lowers the power consumption of the SMO gas sensor. As illustrated in Fig. 1A, the olfactory neuron modules are developed by serially connecting an ovonic threshold switch (OTS) and a micro–light-emitting diode (μLED) platform–based SMO gas sensor. In this study, the OTS is composed of a GeSe film with a threshold switching voltage of ~2.0 V (*32*). For the gas sensor, the Au and Ag nanoparticle (NP)–decorated In_2O_3 thin films are integrated into an ultraviolet (UV) μLED platform, with a power consumption of tens to hundreds of microwatts (*16*). Figure 1 (B and C) illustrates the neuron operation of the OTS by switching between the high-resistance state (HRS) and the low-resistance state (LRS), as well as the spiking characteristics of the olfactory neuron module for various gas types. Notably, the spiking characteristics are collected in the transient region, where the gas sensor reacts with the target gases, making it possible to conduct data augmentation for real-time gas classification with an accuracy of 99.6%. Furthermore, Fig. 1D shows that coriander and culantro spices are accurately classified under humidity disturbance conditions, demonstrating a practical application of the proposed system.

RESULTS

Characteristics of an OTS neuron

Figure 2 shows the characteristics of the OTS neuron. The OTS was fabricated on a W plug–patterned substrate with a 135-nm-diameter contact hole, where the GeSe active layer was deposited using atomic layer deposition. Figure 2A shows that the GeSe layer is sandwiched between a top TiN electrode and a bottom W electrode. The cross-sectional transmission electron microscope (TEM) image in Fig. 2B reveals that a 40-nm GeSe layer was conformally deposited. Figure S1 and Materials and Methods provide the detailed fabrication procedures. Figure S2 shows the cross-sectional energy-dispersive spectrum (EDS) mapping data of GeSe-based OTS. Auger electron spectroscopy data indicate that the atomic concentration ratio of Ge to Se was 6:4, which is suitable for stable neuron operation with superior endurance characteristics over 10^6 cycles under a set (switch-on) pulse amplitude of 2.5 V (fig. S3) (*32*). Figure 2C shows the current-voltage (*I-V*) characteristics, highlighting the threshold switching behavior. Amorphous chalcogenides in OTS contain numerous defects that trap electrons and hinder their movement (*32*–*36*). When an electric field is applied to amorphous chalcogenide films, the energy of electrons increases,

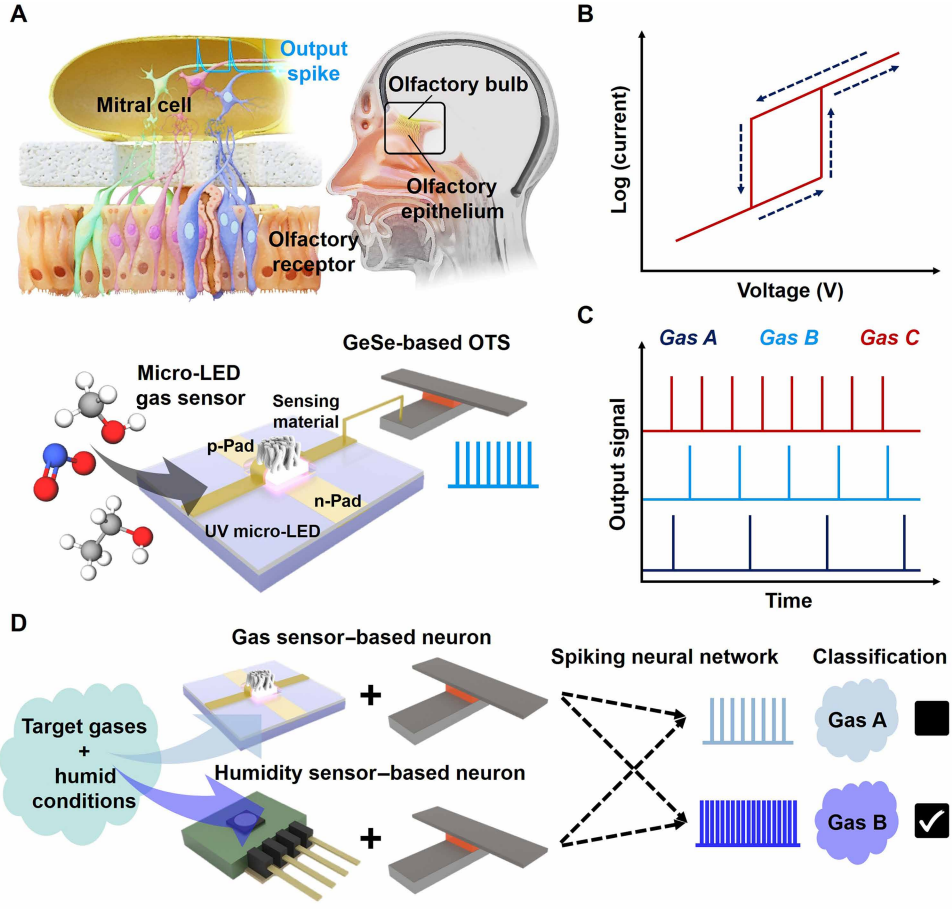


Fig. 1. Schematic of the artificial olfactory neuron module mimicking a biological olfactory system and the practical application of the artificial olfaction system. (**A**) Schematic representation of the biological olfactory system and artificial olfactory neuron module, connecting a GeSe-based OTS and μLED platform–based SMO gas sensors in series. (**B**) Threshold switching characteristics of the OTS showing its transition from an HRS to an LRS when the applied voltage exceeds the threshold voltage (V_{th}). (**C**) Schematic of spike signals generated from the module for different target gases. The spiking frequency varies depending on the target gas because of changes in the resistance of the SMO. (**D**) Schematic of the gas classification under different humidity conditions using the gas sensor–based neuron and humidity sensor–based neuron as the input neurons of the hardware-based SNN.

Downloaded from https://www.science.org at Korea University on September 28, 2025

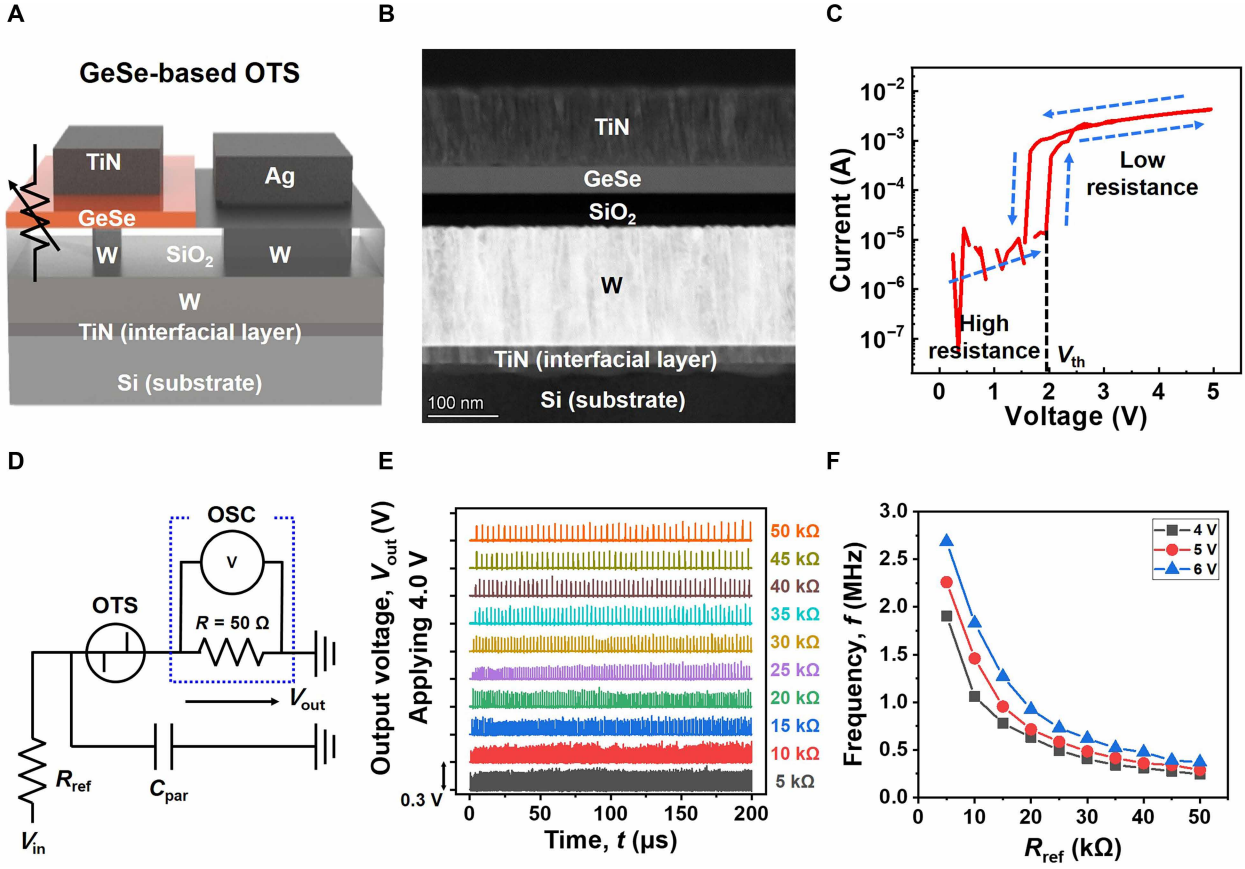


Fig. 2. Characteristics of the GeSe-based OTS neuron. (**A**) Schematic diagram and (**B**) cross-sectional TEM image of the OTS. (**C**) Current-voltage (*I-V*) characteristics representing the threshold switching behavior. (**D**) Experimental setup for the spiking characteristics measurement. The output voltage (V_{out}) was measured by an OSC serially connected to the OTS. Ω, ohms. (**E**) V_{out} over time under various reference resistance (R_{ref}) values. kΩ, kilohms. (**F**) Extracted spiking frequency (*f*) versus R_{ref} under various input voltage (V_{in}) values.

and hopping conduction is activated, forming a conduction path. Once the applied voltage exceeds a threshold voltage (V_{th}), a sudden transition to the LRS occurs, a phenomenon known as threshold switching, which enables neuronal firing operation (*34*, *37*). Notably, V_{th} was only 2 V, substantially lower than that of a MOSFET-based neuron (~5 V) in the previously reported olfactory study, which is required to induce impact ionization for threshold switching (*29*). This lower V_{th} decreases the operation voltage and power consumption of the olfactory neuron module. It should be noted that doping techniques can further decrease the V_{th} of the OTS (*38*, *39*).

Figure 2D illustrates the experimental setup used to measure the spiking characteristics of the OTS neuron. A reference resistor and an oscilloscope (OSC) were connected in series to the OTS device's top and bottom electrodes, respectively. The output voltage (V_{out}) was measured, while an input voltage (V_{in}) was applied to the reference resistor, and the OSC was grounded. As V_{in} was applied, the current flowed into the OTS through the reference resistor, causing charges to accumulate at the parasitic capacitor, thereby increasing the voltage across the OTS. This process represents the neuron's integration process. It should be noted that given that a cable connects the OTS and the reference resistor, the presence of a parasitic capacitor (~450 pF) is inevitable. Once the voltage across the OTS reaches V_{th} and the HRS changes to the LRS, the accumulated charges are rapidly discharged toward the OSC, representing the neuron's firing process. Once the accumulated charges are fired, the voltage across the OTS decreases, causing it to return to the HRS.

Consequently, continuous spike-shaped V_{out} signals can be observed on the OSC when a constant V_{in} is applied. Figure 2E shows the measured V_{out} over time (spiking characteristics) under different reference resistance (R_{ref}) values when V_{in} was 4 V, following the aforementioned mechanism. As R_{ref} decreased, the spiking frequency (*f*) increased because of the higher current applied to the OTS, which accelerated charge accumulation at the parasitic capacitor. Figure 2F shows the extracted primary frequency, *f*, obtained from the fast Fourier transform versus R_{ref} at various V_{in} values (*27*). For a fixed R_{ref}, *f* increases as V_{in} increases because of the increased current and faster charge accumulation at the parasitic capacitor. Figure S4 shows the spiking characteristics under V_{in} values of 5 and 6 V.

Performances of an SMO-integrated μLED gas sensor

A μLED gas sensor with a power consumption of ~0.1 mW was adopted to minimize the total power consumption of the olfactory neuron module (*16*, *18*). Traditional Joule heating–based methods activate SMO at 200° to 500°C but consume high power. Microelectromechanical system–based microheaters (e.g., suspended bridges,

Downloaded from https://www.science.org at Korea University on September 28, 2025

cantilevers, and self-heating nanowires) reduce heat loss and operate at 1 to 10 mW but still face power issues, fatigue failure, and structural fragility. To overcome these limitations, we fundamentally shifted from thermal activation to photoactivation by using a μLED-based sensor. Figure 3A presents the schematic illustration of the gallium nitride (GaN)–based μLED fabricated using microfabrication processes, followed by insulation with SiO_2 and patterning of the interdigitated electrode (IDE) (fig. S5). The μLED acts as a light source to optically stimulate the SMO sensing layer. A μLED with a size of 50 μm by 50 μm, emitting UV light at a wavelength of 395 nm, was fabricated. Porous In_2O_3 films were deposited onto the IDE using a glancing angle deposition (GLAD) method, as shown in Fig. 3B. The working mechanism of this chemoresistor sensor is related to the change in depletion layer thickness and accompanying electrical resistance change when the target gas is adsorbed (*40*–*42*). Two different sensing materials were used by coating the surface of the In_2O_3 films with plasmonic metals, specifically Au and Ag NPs, respectively, to maximize sensor sensitivity. The morphology of the NP-coated In_2O_3 (In_2O_3@NPs) material was confirmed using a scanning electron microscope (SEM) and TEM. Figure 3C shows that the thickness of the In_2O_3 film was ~250 nm, and the average diameters of Ag and Au NPs were ~30 and ~10 nm, respectively. EDS mapping confirmed that Ag and Au NPs were well coated on the In_2O_3 surface (fig. S6). Figure 3D illustrates the working principle of the μLED gas sensor. When the UV light is shed onto the SMO, electrons in the valence band can absorb enough energy to overcome the bandgap and transit to the conduction band, generating hot electron-hole pairs (*40*). These carriers enhance the reaction between the SMO surface and the target gas, thereby improving the sensor responses. On the basis of UV-visible spectroscopy measurements of the In_2O_3 films and the corresponding Tauc plot, the optical bandgap energy was determined to be ~3.65 eV, which matches well with the 395-nm UV of the μLED (fig. S7). Furthermore, when photons are incident on the Ag and Au NPs on the In_2O_3 surface, localized surface plasmon resonance (LSPR) is induced, creating a strong electric field and a high concentration of energetic electrons around the NPs (*43*, *44*). These electrons can be transferred from the NPs to the adjacent SMO, supplying extra carriers that can participate in the gas reaction, thereby further enhancing the performance of the μLED gas sensors. Notably, the proximity between the gas

Downloaded from https://www.science.org at Korea University on September 28, 2025

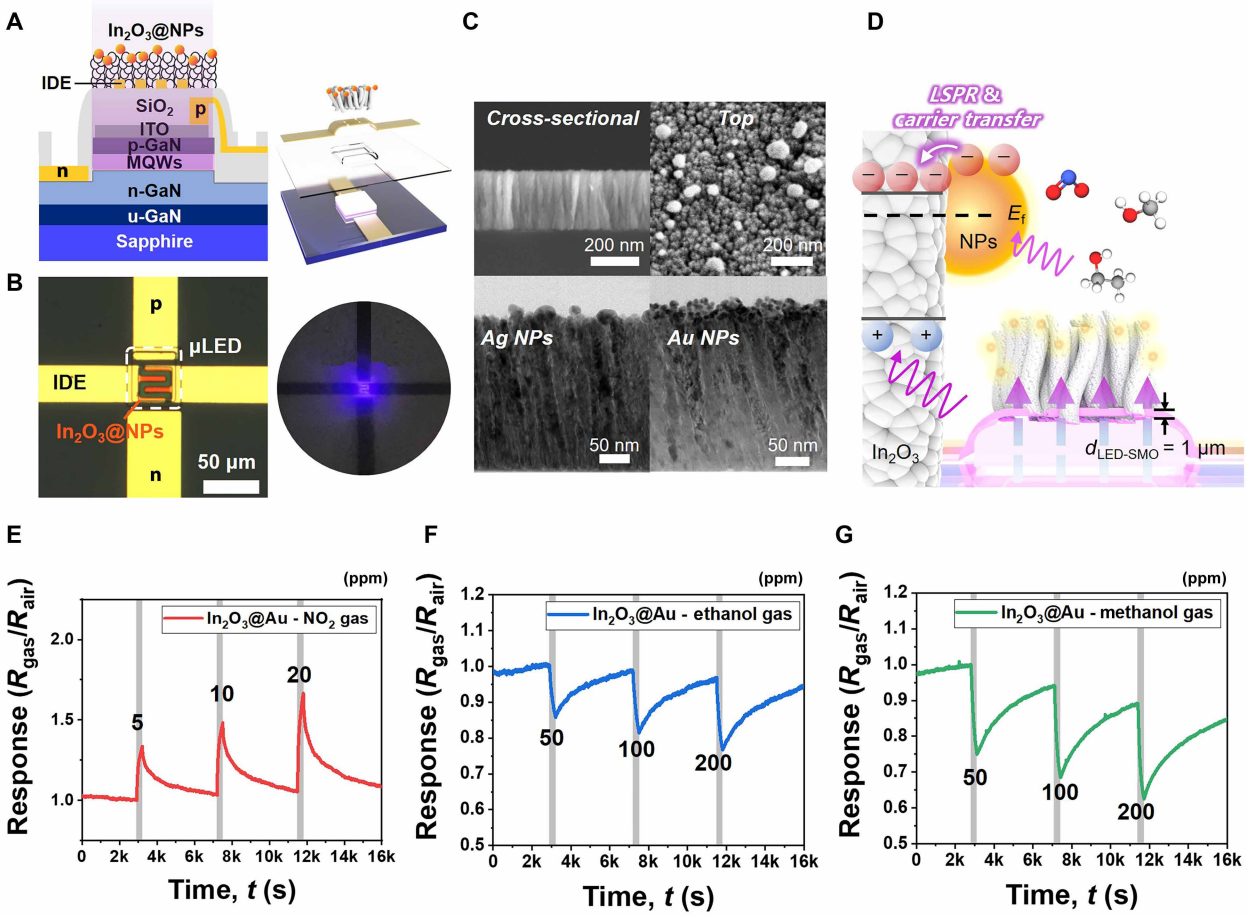


Fig. 3. Characteristics of the In_2O_3@NPs-integrated μLED gas sensor. (**A**) Schematic image of the UV μLED gas sensor. ITO, indium tin oxide; MQWs, multiple quantum wells. (**B**) Optical microscope image of the μLED gas sensor integrated with In_2O_3@NPs and emitting UV light. (**C**) SEM and TEM images of In_2O_3@NPs. (**D**) Gas sensing mechanism of the μLED gas sensor, where extra charge carriers generated by the localized surface plasmon resonance (LSPR) effect of NPs are transferred to In_2O_3, enhancing the gas reaction. Dynamic responses of the In_2O_3@Au-integrated μLED gas sensor to (**E**) NO_2, (**F**) ethanol, and (**G**) methanol gases. Shaded and unshaded areas represent the target gas with specified concentrations and synthetic ambient air, respectively.

sensing layer and the μLED in a monolithic structure (distance, $d_{LED\text{-}SMO} = 1$ μm) minimized the energy loss. Further power saving was achieved by activating only the localized microscale area (*45*). Materials and Methods describes the detailed fabrication and integration process of the μLED sensor, as well as the sensing materials. Figure S7 shows the spectrum and *I-V* curve of the μLED.

In this study, NO_2, ethanol, and methanol gases were used as target gases to evaluate the characteristics of the μLED gas sensor. In_2O_3 is an n-type SMO. Therefore, when the oxidizing NO_2 gas is adsorbed, it attracts electrons from the SMO surface, decreasing electrical conductivity. On the other hand, when the reducing gases, such as ethanol and methanol, are adsorbed, they react with oxygen ions on the SMO surface, releasing electrons and thereby increasing electrical conductivity. Figure 3 (E to G) shows the response of the In_2O_3@Au gas sensor to the three target gases when a forward bias of 3.0 V was applied to the μLED, consuming 213.3 μW. In this study, the optimal operating conditions for the μLED gas sensors were selected by referencing previous literature, considering both power consumption and sensor sensitivity (*16*, *46*, *47*). The response (S) was calculated as R_{gas}/R_{air}, where R_{gas} and R_{air} are the resistances in gas and air, respectively. For 20 parts per million (ppm) of NO_2, 200 ppm of ethanol, and 200 ppm of methanol, the responses of the In_2O_3@Au gas sensor were $S = 1.66$, 0.766, and 0.625, respectively. Figure S8 presents the results of the 10-cycle reproducibility test for three gases. Figure S9 shows the response of the In_2O_3@Ag gas sensor when a forward bias of 2.9 V was applied to the μLED, resulting in a power consumption of 28.0 μW. The responses for 20 ppm of NO_2, 200 ppm of ethanol, and 200 ppm of methanol were $S = 4.62$, 0.955, and 0.835, respectively. Consequently, the μLED gas sensors developed in this study were able to maximize the energy efficiency of the sensing parts, with power consumption tens to hundreds of times lower than that required by heater platform–based gas sensors (*15*, *17*, *48*). This notable power reduction was achieved because, while both heat and light overcome the SMO bandgap, their activation mechanisms differ. Heater-based methods require heating the material to a specific temperature, consuming more power. In contrast, the μLED gas sensor efficiently transfers light energy to a localized area of 50 μm by 50 μm, enabling low-power operation. Table S1 compares state-of-the-art SMO gas sensors activated by heating and photoexcitation in terms of power consumption, response time, and recovery time (*6*, *7*, *15*, *49*–*57*). While our μLED-based sensor does not exhibit the fastest temporal response, as discussed in later sections, its integration with OTS and SNN algorithms enables immediate gas classification, effectively compensating for the slower response speed.

Characteristics of an artificial olfactory neuron

The artificial olfactory neuron module was developed by connecting a GeSe-based OTS neuron and a μLED platform–based gas sensor in series. The sensor system was built by replacing the reference resistor in Fig. 2D with the gas sensor. In this system, given that the OTS neuron is connected in series with the gas sensor, changes in the sensor's resistance modulate the current flowing into the OTS device. This changes the charging speed of the parasitic capacitor, determining how frequently it reaches the threshold voltage and fires spikes. In this study, two types of neuron modules were developed depending on the gas-sensing materials, In_2O_3@Au and In_2O_3@Ag. Three target gases (NO_2, ethanol, and methanol) were used to measure the spiking characteristics of the module in response to each gas. Figure 4 shows the measured spiking characteristics of an In_2O_3@Au gas sensor in response to the target gases. During the measurement of the spiking characteristics, V_{in} was set to 4 V. Materials and Methods provides a detailed explanation of the measurement conditions. Figure 4A shows that f from the module decreased as the concentration of the NO_2 gas increased because the SMO resistance (R_{sens}) increased when the sensor reacted with the NO_2 gas. On the other hand, Fig. 4 (B and C) shows that f increased as the ethanol and methanol gas concentrations increased because R_{sens} decreased when the sensor reacted with these reducing gases.

Figure 3 (D to F) and fig. S9 reveal that the responses of the μLED gas sensors did not immediately converge after the injection of the target gas but showed a transient region. Therefore, the f of the artificial olfactory neuron module changes according to the response of the μLED gas sensor in the transient region, as shown in the dot patterns of Fig. 4 (D to F). Here, the line patterns represent the R_{gas}/R_{air} of the gas sensor for different target gases with various concentrations. It should be noted that using the spiking characteristics that change in the transient region allows real-time gas identification, which will be discussed in the next section.

Figure S10 shows the measured spiking characteristics of the module with the In_2O_3@Ag gas sensor, while Fig. 4 (D to F) shows the results for the In_2O_3@Au gas sensor. The sensing materials of both gas sensors were based on n-type SMO, resulting in a similar overall tendency in the spike responses. Despite this finding, the magnitude of the spike responses differed because the responses of the two gas sensors to the target gases were distinct. Figure 4 and fig. S10 show the overlapping regions in the spike responses of the module even though the types of gases are different, which makes it challenging to classify the gases on the basis of the spike response of only a single neuron module. However, it becomes probable to classify the gases even in the transient region by using different spiking characteristics generated from two different modules.

Figure S11 illustrates the spiking characteristics of the OTS neuron, disconnected from the gas sensor and connected to a R_{ref} of 25 kilohms, where the spike patterns remain nearly identical under various gas conditions. This result demonstrates that the target gases did not directly affect the characteristics of GeSe-based OTS.

The energy consumption was extracted under gas-sensing conditions to confirm the enhanced energy efficiency of the proposed artificial olfactory neuron module. The energy consumption per one spike can be computed by integrating the output current (I_{out}) and V_{in} over time using the following equation

$$E_{neuron} = V_{in} \int_0^{1/f} I_{out} dt$$

I_{out} was calculated by dividing the measured V_{out} from the OSC by the OSC resistance (50 ohms). Figure S12A shows the calculated I_{out} for the neuron module, composed of the In_2O_3@Ag gas sensor and OTS, at an ethanol concentration of 200 ppm. In this study, the V_{in} used to measure the spike characteristics of the artificial olfactory neuron module for each target gas was 4.0 V. As shown in fig. S12B, E_{neuron} corresponding to 12 spikes was calculated to be 23.28 nJ by multiplying V_{in} with I_{out} and integrating over time, resulting in an average E_{neuron} of 1.94 nJ per spike. Table S2 compares the energy consumption of previously reported artificial neuron modules with that of the artificial olfactory neuron module developed in this study.

Downloaded from https://www.science.org at Korea University on September 28, 2025

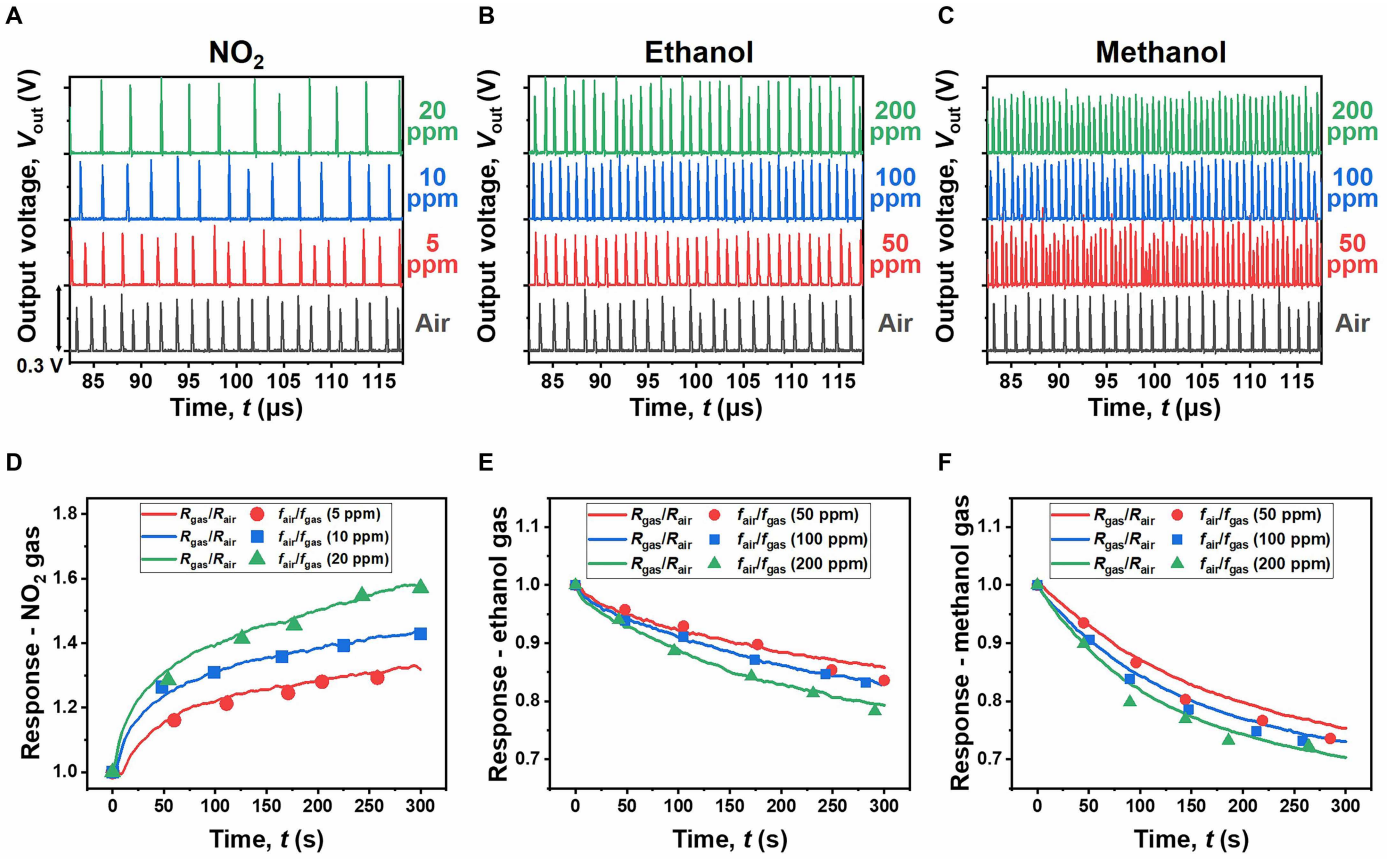


Fig. 4. Spiking characteristics of the artificial olfactory neuron module. Spiking characteristics of the module with the In_2O_3@Au gas sensor when exposed to (**A**) NO_2, (**B**) ethanol, and (**C**) methanol gases. Responses of the gas sensor (line) and the module (dot) in the transient region after the injection of (**D**) NO_2, (**E**) ethanol, and (**F**) methanol gases with various concentrations.

The energy consumption of the proposed module is substantially lower than that of an artificial tactile neuron using an OTS neuron and pressure sensor at 3.54 nJ per spike (*28*). Also, it is lower than the 2.79 nJ per spike reported for the previously described artificial olfactory neuron module using a MOSFET-based neuron (*29*). Furthermore, the power consumption of the μLED was 28.0 μW, which is ~1/460 that of the microheater platform–based gas sensors (*29*). Therefore, it is expected that the energy efficiency of the E-nose can be substantially enhanced by implementing the artificial olfactory neuron module developed in this study.

Real-time gas classification with a software-based SNN

In general, the responses of the gas sensors do not converge immediately after the injection of the target gas. It usually takes a few minutes to classify gases when using the response data after stabilization, hindering real-time analysis. Therefore, this study used the data augmentation method using response data obtained from the olfactory neuron modules in the transient region through curve fitting with a logarithmic function to classify target gases (NO_2, ethanol, and methanol) in real time. Figure 5A shows the data augmentation results using the In_2O_3@Au gas sensor module's response to the NO_2 gas. Using the augmented response data and the response at the air state, f values for each second after the target gas injection were generated. Figure S13 shows the results of data augmentation using the module's response to the reducing gases with the In_2O_3@Au gas sensor. The augmented data were used as input for training and validating a software-based SNN. Figure 5B illustrates the allocation of training and validation data. In this study, the gas-injected region was divided into five regions at 1-min intervals, and each region was further subdivided into five parts. The middle part was used as validation data, while the remaining parts were used as training data. Gas classification was performed for each second to verify the possibility of real-time gas classification for the entire region after gas injection.

Figure 5C illustrates an SNN comprising two input neurons, three hidden layers, and three output neurons for real-time gas classification. Two artificial olfactory neuron modules, composed of the In_2O_3@Au and In_2O_3@Ag gas sensors, each with the OTS neuron, correspond to the two input neurons. Each of the three hidden layers consists of 80 neurons, and the three output neurons correspond to NO_2, ethanol, and methanol gas. The PyTorch code for the SNN was revised from the open access source code developed by Duan *et al.* (*58*). The spikes generated from the input neurons were multiplied by the weights and accumulated in the first hidden layers through the synapse crossbar array. In the first hidden layer, if the output voltage of the neurons that received the accumulated signals exceeded the threshold voltage for firing, those neurons generated spikes. They propagated the spike signals to the following synapse crossbar array and neuron layer. These processes were repeated in each hidden layer of neurons. Finally, the gas was classified on the

Downloaded from https://www.science.org at Korea University on September 28, 2025

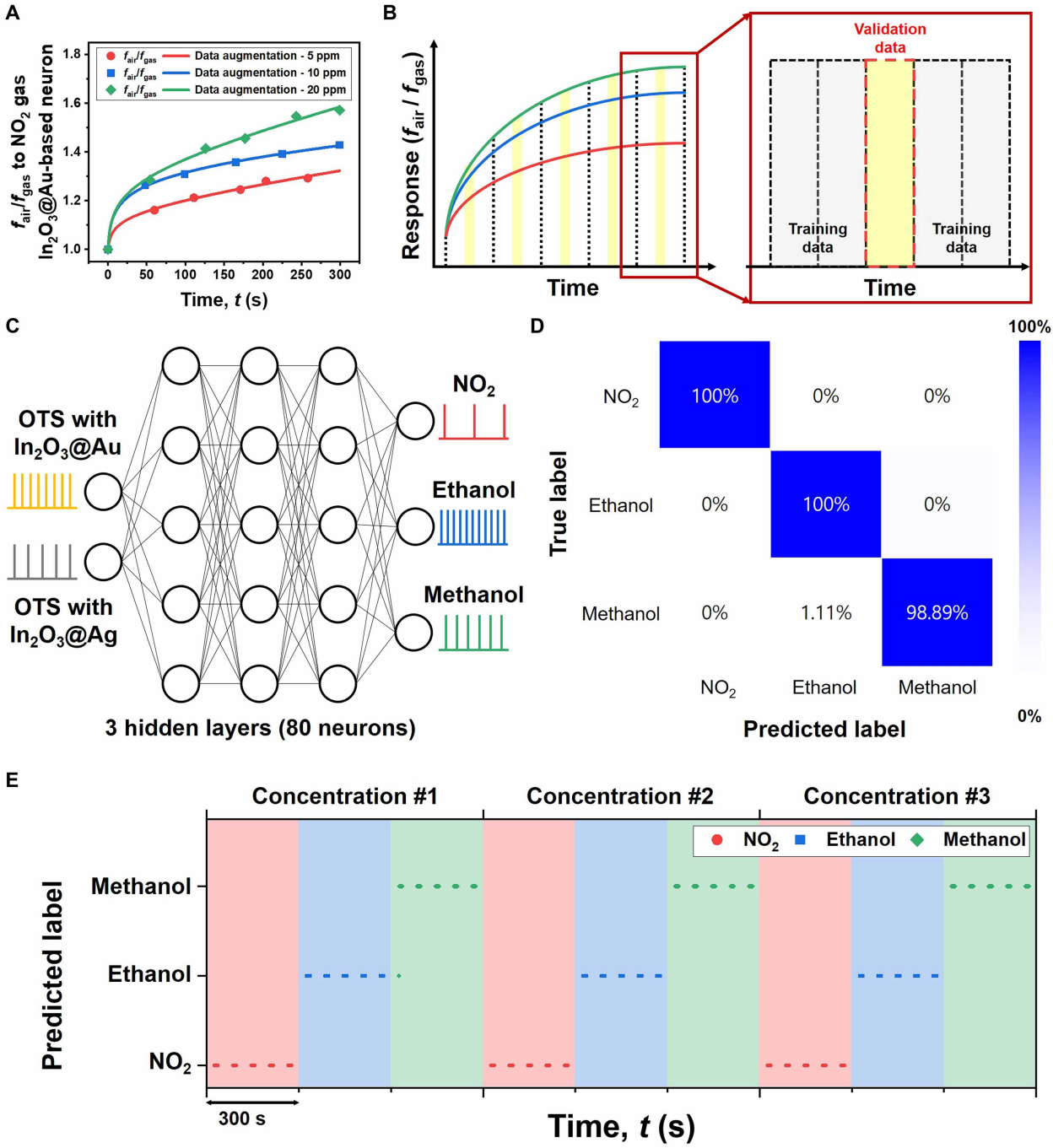


Fig. 5. Real-time gas classification based on software simulation. (**A**) Data augmentation using the response of the neuron module with In_2O_3@Au to NO_2 gas. (**B**) Schematic of the training and validation data allocation, where the gas-injected region was divided into five regions, and each region was further subdivided into five parts. The middle part was used for validation, and the rest was used for SNN training. (**C**) Schematic of the SNN constructed for the real-time gas classification. Two artificial olfactory neuron modules using the In_2O_3@Au and In_2O_3@Ag gas sensors serve as input neurons. Each of the three hidden layers consists of 80 neurons, and the three output neurons correspond to NO_2, ethanol, and methanol gas. (**D**) Confusion matrix of the gas classification results obtained by the SNN from the validation datasets. (**E**) Real-time gas classification results where the symbol position represents the predicted gas type, and the background color indicates the true gas type (red, blue, and green corresponding to NO_2, ethanol, and methanol gases, respectively). The real-time classification was successfully performed with an accuracy of 99.6%.

Downloaded from https://www.science.org at Korea University on September 28, 2025

basis of the output neuron that produced the highest number of spikes. The SNN was trained by backpropagating the error and comparing the predicted and true gas labels. Given that the spike function is nondifferentiable, a sigmoid function was used to extract the spike probability as a continuous value during the backpropagation process. In this study, for the SNN, the synapse weights were distinguished by 128 (2^7 bits) conductance values. The dataset used in the SNN consisted of the spiking characteristics of the modules for three different gases with three different concentrations, with data collected every second for 300 s after gas injection. Among these datasets, 540 were used as validation datasets, and the remaining datasets were used as training datasets.

Figure 5D shows a confusion matrix for gas classification by the SNN using the validation dataset. In this study, real-time classification was performed with an accuracy of 99.6% for various gas types and concentrations. Figure 5E displays the real-time prediction results for gas types across all cases. The colors of the background and the symbol in the graph represent the true gas type label, with red, blue, and green corresponding to NO_2, ethanol, and methanol gases, respectively. The position of the symbols represents the predicted gas type for the validation data, and the concentration of each target gas is expressed as a numerical value, arranged in order of increasing concentration level. Figure 5E demonstrates that the gas classification was performed accurately across the entire region after gas injection, even though it was conducted every second. This result demonstrates that the artificial olfactory neuron module developed in this study enables the implementation of a neuromorphic olfactory system for real-time gas classification while maximizing energy efficiency. To further validate the generalization capability of the proposed approach, we additionally tested the model with NO_2 response data that were not used during training. As shown in fig. S14, data augmentation was also carried out using the responses of the neuron module with In_2O_3@Au and In_2O_3@Ag sensors to NO_2 gas. When these augmented data were input into the pretrained model, real-time classification was successfully achieved with 100% accuracy (fig. S15). Similar tests can be performed for the other two gases (ethanol and methanol); however, because of their more similar response patterns, the classification accuracy can be lower than that achieved with NO_2. Although this study implemented real-time gas classification on the basis of simulation because of the challenges of large-scale integration for a complex network, future research will focus on integrating multiple neurons and synapse arrays into a single chip. This advancement is expected to enable a network capable of reliably performing real-time gas classification at the hardware level.

Spice classification under humidity disturbance conditions with a hardware-based SNN

Ingredient classification was conducted under conditions of humidity disturbance to verify the applicability of the developed artificial olfactory neuron module to food quality and pharmaceutical evaluations. Identifying specific species among various ingredients is crucial in the two applications (*59*, *60*). Traditional E-nose systems have shown reasonable performance, but their high power consumption and hardware costs have hindered their adoption in handheld systems (*60*–*62*). This work demonstrates the potential to overcome these limitations by classifying spices using a fully hardware-based SNN, with a particular focus on distinguishing the smells of coriander and culantro. Figure S16A shows the response of the In_2O_3@Ag gas sensor to the coriander and culantro gases, and the sensor exhibits different responses despite their similar aromas. However, humidity conditions can change in real situations, which may affect the response of SMO gas sensors (*63*–*65*). Figure S16 (B and C) demonstrates that the sensor responds similarly when humidity conditions change despite the differences in species, making classification more challenging.

Figure 6A schematically shows the test setup for measuring the spiking characteristics of the artificial olfactory neuron module with the In_2O_3@Ag gas sensor. The tests were conducted at relative humidities (RHs) of 45 and 60%, with a fixed gas flow rate of 50 standard cubic centimeters per minute (SCCM). Figure 6B shows f generated from the module, and fig. S17 shows the corresponding spiking characteristics of the module. Given that the gas sensor showed similar responses to coriander at an RH of 60% and culantro at an RH of 45%, the f values were almost identical. This result highlights the challenge of distinguishing between the two species using only a single gas sensor–based module under conditions of humidity disturbance. Therefore, a humidity sensor–based neuron module was developed and integrated as an input neuron in the hardware-based SNN to provide humidity information for spice classification (*66*).

This study used a commercial humidity sensor (ETH-01DV, Eco-Narae, Korea) for the humidity sensor–based neuron module. Figure S18A shows the voltage output of the humidity sensor ($V_{H,out}$) for RH levels of 30, 45, and 60% with the spice gas when 2.6 V was applied to the humidity sensor for activation (*67*). To develop the module using the humidity sensor, $V_{H,out}$ must be converted into spike signals. Therefore, the OTS neuron and humidity sensor were connected through a MOSFET (BS107P, Diodes Incorporated, US) to transmit current to the OTS. It should be noted that when $V_{H,out}$ from the humidity sensor is applied directly to the OTS, the voltage across the OTS remains fixed at $V_{H,out}$, preventing spiking operation. Figure S18 (B and C) illustrates the spiking characteristics when the OTS was connected to the drain of the MOSFET, with 1.3 and 1.5 V applied to the gate of the MOSFET, respectively. As the voltage applied to the MOSFET gate increases, more current flows in the direction of being drawn out from the OTS, rapidly charging the parasitic capacitor. Therefore, it was confirmed that the spiking frequency is higher when a larger voltage is applied to the gate. Figure 6C illustrates a circuit diagram for measuring the spiking characteristics of the humidity sensor–based neuron module, while Fig. 6D displays the corresponding spiking characteristics. Given that the output spike signals of the humidity sensor–based neuron module were determined by $V_{H,out}$, the f at an RH of 60% was higher than that at an RH of 45% regardless of the species. Consequently, the humidity sensor–based neuron module was developed without the need for any additional conversion circuits.

Figure 6E illustrates a circuit diagram of the hardware-based SNN for spice classification under conditions of humidity disturbance. The In_2O_3@Ag gas sensor–based neuron module and humidity sensor–based neuron module were used as input neurons. A hybrid of a stand-alone transistor and single-typed resistor (1T1R) structure was used for synapses (*68*). A commercial MOSFET (LND150N3-G, Microchip Technology, US) and resistors were integrated onto a printed circuit board (PCB) for synapse implementation. The synaptic weight was determined by the resistance of the 1T1R synapse, which functions as a weight storage element. This weight can be modulated when a resistive memory device, such as a memristor, is used as the

Downloaded from https://www.science.org at Korea University on September 28, 2025

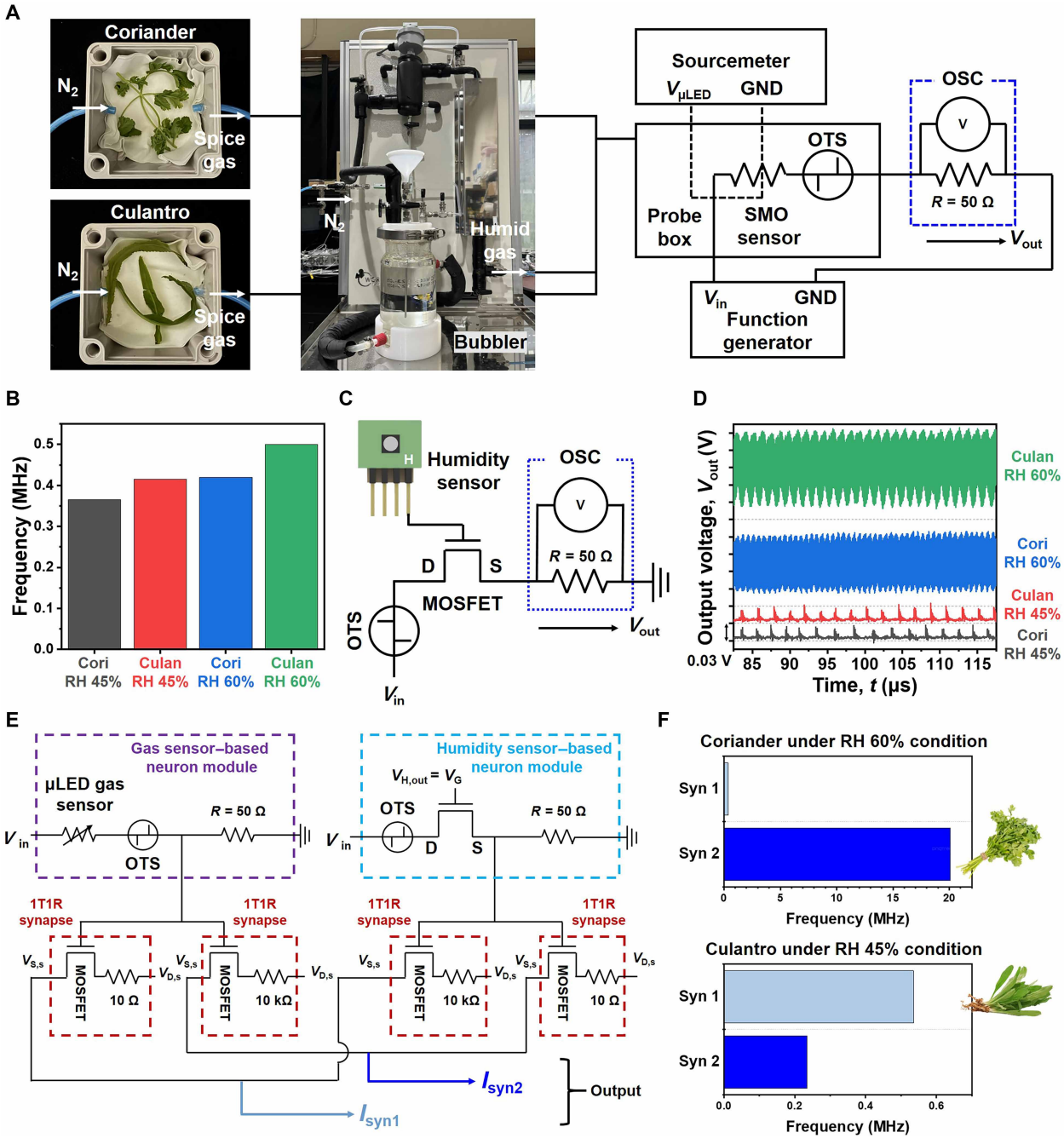


Fig. 6. Fully hardware-based SNN for spice classification under humidity disturbance conditions. (**A**) Schematic illustration of the test setup for measuring the spikes of the gas sensor–based neuron module in response to coriander and culantro gases under different humidity conditions. (**B**) Spiking frequency generated by the In_2O_3@Ag gas sensor–based neuron module in response to spice gases under 45 and 60% RH conditions. (**C**) Circuit diagram and experimental setup for measuring spiking characteristics of the humidity sensor–based neuron module. (**D**) Spiking characteristics of the humidity sensor–based neuron module in response to spice gas under different humidity conditions, specifically RHs of 45 and 60%. (**E**) Circuit diagram of the hardware-based SNN for spice classification under humidity disturbance conditions. The gas sensor–based neuron module and humidity sensor–based neuron module were used as input neurons for the SNN. When the spiking frequency of output 1 exceeded that of output 2, it was classified as culantro; otherwise, it was classified as coriander. (**F**) Spiking frequencies of the collected current spike signals at the output layer in coriander gas under the 60% RH condition and culantro gas under the 45% RH condition.

Downloaded from https://www.science.org at Korea University on September 28, 2025

resistor. Synapses with lower resistance transmit signals more strongly (high weight), while those with higher resistance transmit signals more weakly (low weight). In the SNN, the synapse between the gas sensor–based neuron module and the first output neuron (Output 1) had a lower resistance, and the connection to the second output neuron (Output 2) had a higher resistance. Conversely, the humidity sensor–based neuron module had the opposite configuration. In this study, classification was conducted only for coriander at an RH of 60% and culantro at an RH of 45%, where the spiking characteristics of the artificial olfactory neuron module were almost identical. The classification was determined by comparing the *f* values of output neurons: If the *f* of output 1 exceeded that of output 2, the gas was classified as culantro; otherwise, it was classified as coriander. Figures S19 and S20 show the spiking characteristics of the synaptic current collected from the output neurons (I_{syn}), and the *f* values of output neurons are shown in Fig. 6F. First, when the coriander gas under an RH of 60% was injected, the *f* of output 2 was higher than that of output 1, leading to the correct classification as coriander. On the other hand, when culantro gas under an RH of 45% was injected, the *f* of output 1 was higher than that of output 2, leading to its correct classification as culantro. These results demonstrate that the hardware-based SNN accurately classified similar spices even under humidity disturbance conditions, achieving adequate humidity compensation for spice classification.

DISCUSSION

This study developed a low-power artificial olfactory neuron module using GeSe-based OTS, which operates at a low voltage of 2.0 V, and an ultralow-power μLED–based SMO gas sensor, which operates at the microwatt level. It could mimic biological olfactory neurons by detecting gases and generating spikes in response. Furthermore, it could substantially decrease power consumption compared to artificial sensory neuron modules developed in other studies. These characteristics were adopted to implement a neuromorphic olfaction system capable of transmitting spike signals without relying on the von Neumann computing architecture, thereby substantially decreasing the hardware cost and power consumption of conventional E-nose systems. Consequently, real-time gas classification was possible for three types of target gases with an accuracy of 99.6% by using the sensor modules as the input neurons of the software-based SNN. In addition, a hardware-based SNN was implemented using an extra-humidity sensor–based neuron module, allowing for the classification of the spice under humidity disturbance conditions. This performance verified the practical applicability of the neuromorphic olfaction system.

Despite the notable achievements of the neuromorphic olfaction system developed in this study, several limitations still need to be addressed. The SNNs face challenges in performing regression because they are based on temporal encoding, where the frequency of discrete spikes represents information. This issue makes it difficult to achieve the continuous output required for regression, which is necessary to identify the gas concentration. Several works accomplished the regression tasks using SNNs through a population voting mechanism, where the outputs of multiple neurons are averaged to decode spike information into continuous values (*69*). By using this mechanism, it will be possible to implement an SNN-based artificial olfaction system capable of both classifying gas types and predicting concentrations.

Also, the hardware-based SNN may be unsuitable for classifying many target gases because of its simple network structure, which limits its ability to effectively train on the complex patterns required for distinguishing between different gas types. Therefore, implementing a large-scale integration of neuromorphic components in the hardware-based SNN that includes sensory neurons, hidden/output neurons, and synapses can enhance the scalability and practicality of the neuromorphic olfaction system.

In summary, the proposed neuromorphic olfaction system is expected to notably improve the functionality and versatility of internet of things–based mobile gas sensor systems by enhancing energy efficiency. This enhancement will make technology more adaptable to various environments, opening up further possibilities for advanced applications.

MATERIALS AND METHODS

Fabrication of the OTS neuron

GeSe deposition was carried out on a W plug–patterned substrate with a 135-nm contact hole using a showerhead-type atomic layer deposition reactor, with $Ge\{N[Si(CH_3)_3]_2\}_2$ and $[(CH_3)_3Si]_2Se$ serving as the Ge and Se precursors, respectively. The precursor vapors were transported into the reactor using Ar carrier gas at flow rates of 100 SCCM for Ge and 50 SCCM for Se. Ar (200 SCCM) was introduced immediately after the precursor injection sequence to remove excess precursors and by-products. The TiN film for the electrode was prepared by sputtering using an Applied Materials Endura 5500 system. Further details on the fabrication process are provided in previous work (*32*).

Fabrication of the μLED gas sensor

The μLED gas sensor was fabricated using a wafer-scale microfabrication process, starting with a GaN layer grown on a sapphire wafer via metal-organic chemical vapor deposition, which emits UV light at a peak wavelength of 395 nm. First, lateral μLEDs with dimensions of 50 μm by 50 μm were fabricated using microfabrication processes that involved reactive ion etching, lithography, and e-beam evaporation. The μLEDs were then insulated with a 1-μm-thick double layer of SiO_2, deposited via plasma-enhanced chemical vapor deposition. Subsequently, a 200-nm-thick gold IDE was patterned on the μLED. The porous In_2O_3 was deposited on the IDE using the GLAD method with a radio frequency sputtering system. Before the GLAD process, a photoresist (AZ 5214, MicroChemicals, Germany) was patterned on the prefabricated μLED to define the sensing area. The GLAD conditions included an argon atmosphere at 4 mtorr, a tilt angle of 85°, a rotation speed of 3.6 rpm, a radio frequency power of 250 W, and a duration of 90 min. Last, Au and Ag NPs were deposited onto the surface of the In_2O_3 film via e-beam evaporation, each with a thickness of 2 nm. Subsequently, the In_2O_3@NPs were patterned using a liftoff process in acetone.

Characterization of materials for the OTS and μLED gas sensor

For measuring the atomic concentration ratio of Ge to Se, Auger electron spectroscopy (ULVAC-PHI, PHI-700) depth profile analysis was used. The cross-sectional images and EDS mapping of the OTS and In_2O_3@NPs were taken with a TEM (Tecnai G2 F30 S-TWIN, FEI, The Netherlands) and a dual-beam focused ion beam system (Helios NanoLab, FEI, The Netherlands). The nanostructures of In_2O_3@NPs

Downloaded from https://www.science.org at Korea University on September 28, 2025

were examined using an ultrahigh-resolution field emission SEM (UHR FE-SEM SU8230, Hitachi, Japan). The absorbance of the In_2O_3 film was analyzed using a UV-visible spectrophotometer (Lambda 1050, PerkinElmer, US). The In_2O_3 film was deposited on 1 cm by 1 cm–sized quartz substrates to measure the absorbance.

Electrical characterization

The threshold switching behavior of OTS neurons was measured using a semiconductor parameter analyzer (Keysight B1500A). The electrical characteristics of the μLED SMO gas sensor were measured using a dual-channel sourcemeter (2636B, Keithley, US). The pulse input voltage of 4 V was applied to neuron modules for 200 μs using a function generator (33210A, Agilent, US). The spiking characteristics of the modules were measured using an OSC (MDO3022, Tektronix, USA).

Gas test setup

The μLED gas sensor was mounted on a PCB using epoxy and connected to the PCB via gold wire bonding. The SMO material integrated into the μLED sensor was connected in series with the OTS through the electrical cable, replacing the reference resistor. The target gases used in the experiment (NO_2, ethanol, and methanol) were controlled at precise flow rates by a mass flow controller (AFC500, ATOVAC, Korea). Each spice gas was placed in a chamber, and N_2 gas was injected into each chamber through the mass flow controller to control the amount of the injected spice gases. In the humidity test, N_2 gas was injected into a bubbler to adjust the humidity conditions in the chamber where the gas sensor was located.

Software-based simulation

An SNN simulation was implemented using PyTorch software to perform a real-time gas classification. The spiking frequencies based on the measured responses of the artificial olfactory neuron modules to the target gases in the transient region were applied to the SNN simulation. The SNN consists of two input neurons and three hidden layers, each containing 80 and 3 output neurons. The input neurons correspond to the two types of artificial olfactory neuron modules, and the output neurons correspond to the three types of target gases. The validation data were allocated to ensure uniform distribution across the entire area after the target gas injection. The gas was classified on the basis of the output neuron with the highest spike frequency after 60 epochs.

Supplementary Materials

This PDF file includes:

Figs. S1 to S20
Tables S1 and S2

REFERENCES AND NOTES

1. Q. Li, W. Zeng, Y. Li, Metal oxide gas sensors for detecting NO_2 in industrial exhaust gas: Recent developments. *Sens. Actuators B Chem.* **359**, 131579 (2022).
2. X. Wang, H. Feng, T. Chen, S. Zhao, J. Zhang, X. Zhang, Gas sensor technologies and mathematical modelling for quality sensing in fruit and vegetable cold chains: A review. *Trends Food Sci. Technol.* **110**, 483–492 (2021).
3. B. Lee, J. Lee, J. O. Lee, Y. Hwang, H. K. Bahn, I. Park, S. Jheon, D. S. Lee, Breath analysis system with convolutional neural network (CNN) for early detection of lung cancer. *Sens. Actuators B Chem.* **409**, 135578 (2024).
4. G. Neri, First fifty years of chemoresistive gas sensors. *Chemosensors* **3**, 1–20 (2015).
5. A. Dey, Semiconductor metal oxide gas sensors: A review. *Mater. Sci. Eng. B* **229**, 206–217 (2018).
6. I. Cho, K. Kang, D. Yang, J. Yun, I. Park, Localized liquid-phase synthesis of porous SnO_2 nanotubes on MEMS platform for low-power, high performance gas sensors. *ACS Appl. Mater. Interfaces* **9**, 27111–27119 (2017).
7. I. Cho, Y. C. Sim, M. Cho, Y. H. Cho, I. Park, Monolithic micro light-emitting diode/metal oxide nanowire gas sensor with microwatt-level power consumption. *ACS Sens.* **5**, 563–570 (2020).
8. X. Qiao, Y. Xu, K. Yang, J. Ma, C. Li, H. Wang, L. Jia, Mo doped $BiVO_4$ gas sensor with high sensitivity and selectivity towards H_2S. *Chem. Eng. J.* **395**, 125144 (2020).
9. H. Park, J. H. Kim, D. Vivod, S. Kim, A. Mirzaei, D. Zahn, C. Park, S. S. Kim, M. Halik, Chemical-recognition-driven selectivity of SnO_2-nanowire-based gas sensors. *Nano Today* **40**, 101265 (2021).
10. M. Tonezzer, Selective gas sensor based on one single SnO_2 nanowire. *Sens. Actuators B Chem.* **288**, 53–59 (2019).
11. N. X. Thai, M. Tonezzer, L. Masera, H. Nguyen, N. Van Duy, N. D. Hoa, Multi gas sensors using one nanomaterial, temperature gradient, and machine learning algorithms for discrimination of gases and their concentration. *Anal. Chim. Acta* **1124**, 85–93 (2020).
12. S. Y. Park, Y. Kim, T. Kim, T. H. Eom, S. Y. Kim, H. W. Jang, Chemoresistive materials for electronic nose: Progress, perspectives, and challenges. *InfoMat* **1**, 289–316 (2019).
13. I. Gaillard, S. Rouquier, D. Giorgi, Olfactory receptors. *Cell. Mol. Life Sci.* **61**, 456–469 (2004).
14. D. H. Gire, K. M. Franks, J. D. Zak, K. F. Tanaka, J. D. Whitesell, A. A. Mulligan, R. Hen, N. E. Schoppa, Mitral cells in the olfactory bulb are mainly excited through a multistep signaling path. *J. Neurosci.* **32**, 2964–2975 (2012).
15. M. Kang, I. Cho, J. Park, J. Jeong, K. Lee, B. Lee, D. Del Orbe Henriquez, K. Yoon, I. Park, High accuracy real-time multi-gas identification by a batch-uniform gas sensor array and deep learning algorithm. *ACS Sens.* **7**, 430–440 (2022).
16. K. Lee, I. Cho, M. Kang, J. Jeong, M. Choi, K. Y. Woo, K. J. Yoon, Y. H. Cho, I. Park, Ultra-low-power E-nose system based on multi-micro-LED-integrated, nanostructured gas sensors and deep learning. *ACS Nano* **17**, 539–551 (2023).
17. D. D. Orbe Henriquez, M. Kang, I. Cho, J. Choi, J. Park, O. Gul, J. Ahn, D. S. Lee, I. Park, Low-power multi-transduction nanosensor array for accurate sensing of flammable and toxic gases. *Small Methods* **7**, e2201352 (2023).
18. I. Cho, K. Lee, Y. C. Sim, J. S. Jeong, M. Cho, H. Jung, M. Kang, Y. H. Cho, S. C. Ha, K. J. Yoon, I. Park, Deep-learning-based gas identification by time-variant illumination of a single micro-LED-embedded gas sensor. *Light Sci. Appl.* **12**, 95 (2023).
19. F. Zhou, Y. Chai, Near-sensor and in-sensor computing. *Nat. Electron.* **3**, 664–671 (2020).
20. D. Kwon, G. Jung, W. Shin, Y. Jeong, S. Hong, S. Oh, J. H. Bae, B. G. Park, J. H. Lee, Low-power and reliable gas sensing system based on recurrent neural networks. *Sens. Actuators B Chem.* **340**, 129258 (2021).
21. J. K. Han, S. Y. Yun, S. W. Lee, J. M. Yu, Y. K. Choi, A review of artificial spiking neuron devices for neural processing and sensing. *Adv. Funct. Mater.* **32**, 2204102 (2022).
22. J. Yu, Y. Wang, S. Qin, G. Gao, C. Xu, Z. Lin Wang, Q. Sun, Bioinspired interactive neuromorphic devices. *Mater. Today* **60**, 158–182 (2022).
23. J. H. Yoon, Z. Wang, K. M. Kim, H. Wu, V. Ravichandran, Q. Xia, C. S. Hwang, J. J. Yang, An artificial nociceptor based on a diffusive memristor. *Nat. Commun.* **9**, 417 (2018).
24. J. K. Han, D. M. Geum, M. W. Lee, J. M. Yu, S. K. Kim, S. Kim, Y. K. Choi, Bioinspired photoresponsive single transistor neuron for a neuromorphic visual system. *Nano Lett.* **20**, 8781–8788 (2020).
25. Q. Wu, B. Dang, C. Lu, G. Xu, G. Yang, J. Wang, X. Chuai, N. Lu, D. Geng, H. Wang, L. Li, Spike encoding with optic sensory neurons enable a pulse coupled neural network for ultraviolet image segmentation. *Nano Lett.* **20**, 8015–8023 (2020).
26. J. K. Han, S. C. Park, J. M. Yu, J. H. Ahn, Y. K. Choi, A bioinspired artificial gustatory neuron for a neuromorphic based electronic tongue. *Nano Lett.* **22**, 5244–5251 (2022).
27. J. Lee, S. Kim, S. Park, J. Lee, W. Hwang, S. W. Cho, K. Lee, S. M. Kim, T. Y. Seong, C. Park, S. Lee, H. Yi, An artificial tactile neuron enabling spiking representation of stiffness and disease diagnosis. *Adv. Mater.* **34**, 2201608 (2022).
28. T. Wang, X. X. Wang, J. Wen, Z. Y. Shao, H. M. Huang, X. Guo, A bio-inspired neuromorphic sensory system. *Adv. Intell. Syst.* **4**, 2200047 (2022).
29. J. K. Han, M. Kang, J. Jeong, I. Cho, J. M. Yu, K. J. Yoon, I. Park, Y. K. Choi, Artificial olfactory neuron for an in-sensor neuromorphic nose. *Adv. Sci.* **9**, 2106017 (2022).
30. S. W. Lee, M. Kang, J. K. Han, S. Y. Yun, I. Park, Y. K. Choi, An artificial olfactory sensory neuron for selective gas detection with in-sensor computing. *Device* **1**, 100063 (2023).
31. J. K. Han, Y. K. Choi, M. Seo, W. K. Kim, M. S. Kim, S. Y. Kim, M. S. Kim, G. J. Yun, G. B. Lee, J. M. Yu, Mimicry of excitatory and inhibitory artificial neuron with leaky integrate-and-fire function by a single MOSFET. *IEEE Electron Device Lett.* **41**, 208–211 (2020).
32. C. Yoo, W. Kim, J. W. Jeon, E. S. Park, M. Ha, Y. K. Lee, C. S. Hwang, Atomic layer deposition of Ge_xSe_{1-x} thin films for endurable ovonic threshold selectors with a low threshold voltage. *ACS Appl. Mater. Interfaces* **12**, 23110–23118 (2020).
33. D. Adler, H. K. Henisch, S. N. Mott, The mechanism of threshold switching in amorphous alloys. *Rev. Mod. Phys.* **50**, 209–220 (1978).
34. D. Ielmini, Y. Zhang, Analytical model for subthreshold conduction and threshold switching in chalcogenide-based memory devices. *J. Appl. Phys.* **102**, 054517 (2007).

Downloaded from https://www.science.org at Korea University on September 28, 2025

35. D. Ielmini, Threshold switching mechanism by high-field energy gain in the hopping transport of chalcogenide glasses. *Phys. Rev. B* **78**, 035308 (2008).
36. J. W. Jeon, B. Park, Y. H. Jang, S. H. Lee, S. Jeon, J. Han, S. K. Ryoo, K. Do Kim, S. K. Shim, S. Cheong, W. Choi, G. Jeon, S. Kim, C. Yoo, J. K. Han, C. S. Hwang, Vertically stackable ovonic threshold switch oscillator using atomic layer deposited $Ge_{0.6}Se_{0.4}$ film for high-density artificial neural networks. *ACS Appl. Mater. Interfaces* **16**, 15032–15042 (2024).
37. M. Lee, M. Lee, S. W. Cho, S. W. Cho, S. J. Kim, S. J. Kim, J. Y. Kwak, H. Ju, Y. Yi, B. K. Cheong, S. Lee, S. Lee, Simple artificial neuron using an ovonic threshold switch featuring spike-frequency adaptation and chaotic activity. *Phys. Rev. Appl.* **13**, 064056 (2020).
38. N. S. Avasarala, B. Govoreanu, K. Opsomer, W. Devulder, S. Clima, C. Detavernier, M. Van Der Veen, J. Van Houdt, M. Henys, L. Goux, G. S. Kar, "Doped GeSe materials for selector applications," in *2017 47th European Solid-State Device Research Conference (ESSDERC)* (IEEE, 2017), pp. 168–171.
39. A. Verdy, G. Navarro, V. Sousa, P. Noé, M. Bernard, F. Fillot, G. Bourgeois, J. Garrione, L. Perniola, "Improved electrical performance thanks to Sb and N doping in Se-rich GeSe-based OTS selector devices," in *2017 IEEE International Memory Workshop (IMW)* (IEEE, 2017), pp. 1–4.
40. E. Espid, F. Taghipour, UV-LED photo-activated chemical gas sensors: A review. *Crit. Rev. Solid State Mater. Sci.* **42**, 416–432 (2017).
41. M. E. Franke, T. J. Koplin, U. Simon, Metal and metal oxide nanoparticles in chemiresistors: Does the nanoscale matter? *Small* **2**, 36–50 (2006).
42. Y. F. Sun, S. B. Liu, F. L. Meng, J. Y. Liu, Z. Jin, L. T. Kong, J. H. Liu, Metal oxide nanostructures and their gas sensing properties: A review. *Sensors* **12**, 2610–2631 (2012).
43. C. Clavero, Plasmon-induced hot-electron generation at nanoparticle/metal-oxide interfaces for photovoltaic and photocatalytic devices. *Nat. Photonics* **8**, 95–103 (2014).
44. X. C. Ma, Y. Dai, L. Yu, B. B. Huang, Energy transfer in plasmonic photocatalytic composites. *Light Sci Appl* **5**, e16017 (2016).
45. N. Markiewicz, O. Casals, C. Fabrega, I. Gràcia, C. Cané, H. S. Wasisto, A. Waag, J. D. Prades, Micro light plates for low-power photoactivated (gas) sensors. *Appl. Phys. Lett.* **114**, 053508 (2019).
46. J. D. Prades, R. Jimenez-Diaz, M. Manzanares, F. Hernandez-Ramirez, A. Cirera, A. Romano-Rodriguez, S. Mathur, J. R. Morante, A model for the response towards oxidizing gases of photoactivated sensors based on individual SnO_2 nanowires. *Phys. Chem. Chem. Phys.* **11**, 10881–10889 (2009).
47. M. R. Alenezi, A. S. Alshammari, K. D. G. I. Jayawardena, M. J. Beliatis, S. J. Henley, S. R. P. Silva, Role of the exposed polar facets in the performance of thermally and UV activated ZnO nanostructured gas sensors. *J. Phys. Chem. C* **117**, 17850–17858 (2013).
48. K. Kang, D. Yang, J. Park, S. Kim, I. Cho, H. H. Yang, M. Cho, S. Mousavi, K. H. Choi, I. Park, Micropatterning of metal oxide nanofibers by electrohydrodynamic (EHD) printing towards highly integrated and multiplexed gas sensor applications. *Sens. Actuators B Chem.* **250**, 574–583 (2017).
49. T. Kim, Y. Kim, W. Cho, J.-H. Kwak, J. Cho, Y. Pyeon, J. J. Kim, J. Shin, Ultralow-power single-sensor-based e-nose system powered by duty cycling and deep learning for real-time gas identification. *ACS Sens.* **9**, 3557–3572 (2024).
50. M.-S. Jo, S.-H. Kim, S.-Y. Park, K.-W. Choi, S.-H. Kim, J.-Y. Yoo, B.-J. Kim, Y.-B. Yoon, Fast-response and low-power self-heating gas sensor using metal/metal oxide/metal (MMOM) structured nanowires. *ACS Sens.* **9**, 1896–1905 (2024).
51. B. Lee, I. Cho, M. Kang, D. Yang, I. Park, Thermally/mechanically robust anodic aluminum oxide (AAO) microheater platform for low power chemoresistive gas sensor. *J. Micromech. Microeng.* **33**, 085011 (2023).
52. C.-L. Hsu, L.-F. Chang, T.-H. Hsueh, Light-activated humidity and gas sensing by ZnO nanowires grown on LED at room temperature. *Sens. Actuators B Chem.* **249**, 265–277 (2017).
53. E. Zampettia, A. Bearzotti, A. Macagnano, UV assisted chemical sensor based on electrospun titania nanofibers working at room temperature. *Procedia Eng.* **47**, 912–915 (2012).
54. R. Jaisutti, M. Lee, J. Kim, S. Choi, T.-J. Ha, J. Kim, H. Kim, S. K. Park, Y.-H. Kim, Ultrasensitive room-temperature operable gas sensors using p-Type Na:ZnO nanoflowers for diabetes detection. *ACS Appl. Mater. Interfaces* **9**, 8796–8804 (2017).
55. X.-X. Wang, S. Zhang, Y. Liu, J.-N. Dai, H.-Y. Li, X. Guo, Light-excited chemiresistive sensors integrated on LED microchips. *J Mater Chem A* **9**, 16545–16553 (2021).
56. O. Casals, N. Markiewicz, C. Fabrega, I. Gràcia, C. Cané, H. S. Wasistom, A. Waag, J. D. Prades, A parts per billion (ppb) sensor for NO_2 with microwatt (μW) power requirements based on micro light plates. *ACS Sens.* **4**, 822–826 (2019).
57. G. B. Nam, J.-E. Ryu, T. H. Eom, S. J. Kim, J. M. Suh, S. Lee, S. Choi, C. W. Moon, S. J. Park, S. M. Lee, B. Kim, S. H. Park, J. W. Yang, S. Min, S. Park, S. H. Cho, H. J. Kim, S. E. Jun, T. H. Lee, Y. J. Kim, J. Y. Kim, Y. J. Hong, J.-I. Shim, H.-G. Byun, Y. Park, I. Park, S.-W. Ryu, H. W. Jang, Real-time tunable gas sensing platform based on SnO_2 nanoparticles activated by blue micro-light-emitting diodes. *Nano Micro Lett.* **16**, 261 (2024).
58. Q. Duan, Z. Jing, X. Zou, Y. Wang, K. Yang, T. Zhang, S. Wu, R. Huang, Y. Yang, Spiking neurons with spatiotemporal dynamics and gain modulation for monolithically integrated memristive neural networks. *Nat. Commun.* **11**, 3399 (2020).
59. U. Banach, C. Tiebe, T. Hübert, Multigas sensors for the quality control of spice mixtures. *Food Control* **26**, 23–27 (2012).
60. T. Hübert, C. Tiebe, U. Banach, "Electronic noses for the quality control of spices" in *Electronic Noses and Tongues in Food Science* (Elsevier Inc., 2016), vol. 12, pp. 115–124.
61. M. Kukade, T. Karve, D. Gharpure, "Identification and classification of spices by machine learning," in *2019 IEEE International Conference on Intelligent Systems and Green Technology (ICISGT)* (IEEE, 2019), pp. 1–13.
62. K. K. Pulluri, V. N. Kumar, Qualitative and quantitative detection of food adulteration using a smart E-nose. *Sensors* **22**, 7789 (2022).
63. C. Wang, L. Yin, L. Zhang, D. Xiang, R. Gao, Metal oxide gas sensors: Sensitivity and influencing factors. *Sensors* **10**, 2088–2106 (2010).
64. J. W. Yoon, J. S. Kim, T. H. Kim, Y. J. Hong, Y. C. Kang, J. H. Lee, A new strategy for humidity independent oxide chemiresistors: Dynamic self-refreshing of In_2O_3 sensing surface assisted by layer-by-layer coated CeO_2 nanoclusters. *Small* **12**, 4229–4240 (2016).
65. K. Hwang, J. Ahn, I. Cho, K. Kang, K. Kim, J. Choi, K. Polychronopoulou, I. Park, Microporous elastomer filter coated with metal organic frameworks for improved selectivity and stability of metal oxide gas sensors. *ACS Appl. Mater. Interfaces* **12**, 13338–13347 (2020).
66. M. Kang, I. Cho, N. Park, "Application of deep learning network for humidity compensation of semiconductor metal oxide gas sensors," in *2023 IEEE 36th International Conference on Micro Electro Mechanical Systems (MEMS)* (IEEE, 2023), pp. 799–802.
67. "ETH-01DV temperature & humidity sensor analog output module (DIP)," EcoNarae, p. 3. https://www.icbanq.com/icdownload/data/ICBShop/Board/10.EcoNarae_ETH-01DV.pdf?srsItid=AfmBOoq3W7p1yFmXfD_xSApqKE9rnfxpKAhFLolaKuRHXkyZ0TqdkcJEI.
68. P. Lin, C. Li, Z. Wang, Y. Li, H. Jiang, W. Song, M. Rao, Y. Zhuo, N. K. Upadhyay, M. Barnell, Q. Wu, J. J. Yang, Q. Xia, Three-dimensional memristor circuits as complex neural networks. *Nat. Electron.* **3**, 225–232 (2020).
69. A. Henkes, J. K. Eshraghian, H. Wessels, Spiking neural networks for nonlinear regression. *R. Soc. Open Sci.* **11**, 231606 (2024).

Acknowledgments

Funding: This research was supported by the National Research Foundation of Korea (grant nos. 2020R1A3B2079882 and 2021R1A2C3008742). **Author contributions:** M.K., J.-K.H., and K.L. equally performed all experiments, analyzed the data, and wrote the paper. M.K., J.J., and K.-J.Y. discussed modeling and results of the software-based SNN. C.Y., J.W.J., B.P., W.C., and J.A. contributed to the analysis of the device characteristics. C.S.H. and I.P. supervised the project. All authors have approved the final version of the manuscript. **Competing interests:** The authors declare that they have no competing interests. **Data and materials availability:** All data needed to evaluate the conclusions in this paper are present in the paper and/or the Supplementary Materials.

Submitted 14 January 2025
Accepted 28 August 2025
Published 24 September 2025
10.1126/sciadv.adv9222

Downloaded from https://www.science.org at Korea University on September 28, 2025